

Influence of Bubble Lifetime on the Drying of Catalytically Active Sessile Droplets

Meneka Banik and Ranjini Bandyopadhyay*

Soft Condensed Matter Group, Raman Research Institute, C. V. Raman Avenue,
Sadashivanagar, Bangalore 560080, India.

Corresponding author: *ranjini@rri.res.in

ABSTRACT

When colloidal droplets evaporate, suspended particles are redistributed by a competition between evaporation-driven capillary advection, interfacial Marangoni stresses and particle mobility, leading to diverse deposition patterns relevant to coating and self-assembly. While these mechanisms are well understood for passive suspensions, their interplay in chemically active colloidal systems remains less explored. Here, we investigate the drying dynamics of droplets containing catalytic polystyrene-platinum (PS-Pt) Janus particles in the presence of hydrogen peroxide (H_2O_2) fuel. H_2O_2 undergoes catalytic decomposition at the Pt hemisphere, resulting in the formation of oxygen (O_2). By systematically varying H_2O_2 concentration, surface wettability and open versus confined drying conditions, we identify distinct transport regimes governed by the relative magnitudes of capillary flow and gas bubble-induced Marangoni convection. While time-resolved contact-angle measurements reveal substrate-dependent evaporation modes, an increase in catalytic activity promotes O_2 bubble generation that locally reverses or disrupts outward particle transport. Closed drying conditions further modify evaporation rates and prolong bubble residence times, leading to transitions from peripheral accumulation to spatially uniform or centrally concentrated deposits. Bubble-induced Marangoni flow, controlled here by tuning substrate wettability and environmental conditions, therefore emerges as the dominant mechanism governing the evaporation dynamics and dried morphologies of catalytically active Janus particle droplets.

KEYWORDS:

active particles; capillary advection; colloidal droplets; evaporative self-assembly; Marangoni flow; wettability

INTRODUCTION

The drying of colloidal droplets on flat substrates has long served as a canonical model system for probing interfacial phenomena such as capillarity, wetting transitions and particle transport at confined liquid-vapour interfaces [1-4]. In the classical framework, passive colloidal suspension droplets evaporating under isothermal conditions form ring-like or heterogeneous deposits governed primarily by an outward capillary flux directed toward pinned contact lines [1,2]. Subsequent studies demonstrated that thermal or solutal Marangoni stresses may partially counteract this radial flow, generating internal recirculation that redistributes liquid and suspended particles [5-7]. Together, these principles underpin strategies for producing reproducible coatings, inkjet-printed films, and functional thin layers [8-10]. However, these models rely on the central assumption that suspended particles behave as passive tracers that do not themselves modify the evolving interface or the evaporation pathway [11,12]. This assumption becomes questionable when particles possess intrinsic surface activity or anisotropic interfacial affinity [13].

Janus colloids introduce a fundamentally different scenario, as their chemically asymmetric surfaces interact differently with the liquid-vapour and solid-liquid interfaces [14,15]. For example, in the case of polymer-metal Janus particles, the hydrophilic metal cap and hydrophobic polymeric body generate heterogeneous particle-substrate interactions [16]. As a result, particle adhesion, orientation and mobility at the solid surface become strongly dependent on substrate wettability. This coupling between Janus polarity and surface chemistry introduces a new control parameter absent in passive droplet drying, whereby the substrate no longer serves as a passive boundary but actively selects particle configurations and transport pathways during evaporation [17,18]. These effects are amplified for active Janus particles, which can autonomously perturb the interfacial environment through self-generated chemical fluxes [19].

Wettability governs two inter-related aspects of active Janus particle droplet drying that become tightly coupled as the particles continuously modify their local chemical environment [20]. First, substrate surface energy dictates contact-line mobility and pinning strength, thereby setting the lateral length scale over which interfacial Marangoni stresses (τ_M) can develop [5,21]. Strong pinning constrains stress relaxation and allows surface tension gradients to accumulate, whereas weak pinning permits contact-line motion that partially dissipates these stresses [22,23]. Second, hydrophilic substrates promote droplet spreading into thin precursor

films with shallow curvature and enhanced liquid-air interfacial area [24,25], while hydrophobic substrates preserve curved droplet footprints and their prolonged interfacial residence times [26,27]. Although these distinctions are subtle for passive suspensions, they become critical for Janus systems in which asymmetric particle wettability governs their attachment and detachment dynamics at the substrate.

For catalytically active Janus particle droplets, this substrate wettability dependence determines whether evaporation-driven enrichment or reaction-driven depletion dominates near the contact line [28-30]. Classical evaporation-controlled concentration gradients during passive droplet drying are typically characterised by $\gamma_{edge} < \gamma_{center}$, where γ_{edge} and γ_{center} are the respective surface tensions at the edge and centre of the droplet [5,21]. This scenario requires sustained solute retention and sufficient time for gradients to drive coherent recirculatory flows. In contrast, during the drying of active Janus droplets, localised catalytic consumption at the three-phase boundary generates an inward Marangoni flow, inverts the fuel gradients and biases particle accumulation toward regions of strong particle-substrate affinity [31]. The competition between these mechanisms directly influences particle segregation, clustering propensity and the spatial uniformity of the final deposit. Importantly, these outcomes can arise even in the absence of sustained chemical fluxes, underscoring the dominant role of particle-substrate interactions in determining evaporation pathways [29,32,33]. In polystyrene-platinum (PS-Pt) Janus particle droplets containing H_2O_2 fuel, catalytic decomposition at the Pt cap generates dissolved oxygen (O_2). At higher fuel concentrations, the locally accumulated O_2 nucleates into bubbles, whose residence, growth, and detachment are governed by substrate wettability, environmental conditions, and particle-particle adhesion [6,34,35]. Weakened particle-substrate coupling on hydrophobic surfaces can amplify interfacial mobility and intermittency, while hydrophilic substrates favour stronger droplet pinning and more gradual stress relaxation [36]. Consequently, bubble-mediated perturbations have been viewed as emergent consequences of wettability-controlled interfacial dynamics. [37-39].

In this work, we identify lifetime of O_2 bubbles, generated by catalytic activity at the platinum cap of the Janus particle, as the governing parameter that controls the evaporation pathways of H_2O_2 fueled PS-Pt Janus particle droplets. By systematically varying substrate chemistry, H_2O_2 concentration and open versus confined evaporation environments to control the bubble residence time, we quantify how asymmetric particle-substrate interactions reshape contact-line dynamics, stress relaxation, and particle transport during drying. Time-resolved contact-

angle measurements and final deposit morphologies reveal how Janus polarity couples with substrate wettability to select distinct evaporation modes on hydrophilic and hydrophobic substrates. By establishing the relationships between substrate chemistry, substrate-bubble interactions and active particle assembly, this study provides predictive design rules for coating, printing, and microreactor applications. Broadly, it reframes droplet evaporation as a process governed by interfaces actively shaped by bubble burst and collapse cycles rather than by passive boundary conditions.

MATERIALS AND METHODS

Janus particle synthesis: Polystyrene (PS) microspheres with a mean diameter of 2.07 ± 0.15 μm (Fluorescent PS, Dragon Green, Bangs Laboratories Inc.) were used for Janus particle fabrication. A suspension of PS microspheres was diluted in isopropyl alcohol (IPA, Sigma-Aldrich, $\geq 99.7\%$, FCC, FG) to a final concentration of 0.5 wt%. Clean glass substrates (Blue Star, thickness 1.35 mm) were prepared by sequential ultrasonication in acetone (Sigma-Aldrich, ACS reagent, $\geq 99.5\%$), ethanol (RCP Distilleries India Pvt. Ltd., 99.9%, Analytical Grade), and Milli-Q water (resistivity: 18.2 M Ω .cm at 25 °C, < 5ppb TDS) (15 min each), followed by treatment in piranha solution (3:1 mixture of H₂SO₄, Merck, 98%, for analysis) and H₂O₂ (Thermo Fisher Scientific, 30 wt%). The substrates were rinsed thoroughly with Milli-Q water, dried in a hot air oven, and purged with nitrogen before use. 200 μL of the prepared 0.5 wt.% PS suspension was dispensed onto a cleaned glass slide and kept undisturbed in a clean Petri dish at 25 °C for 8 hours [40]. A close-packed monolayer of PS microspheres, spanning an area of approximately 100 μm^2 , was obtained on the cleaned glass slides by sedimentation. A 20 nm thick platinum (Pt) film was then deposited onto the exposed hemispheres of the PS particles using a benchtop sputter coater (Quorum Q150RS), which resulted in half-coated PS particles. The Janus particles were released from the substrate into Milli-Q water via ultrasonication for 1 minute (Maxsell ultrasonic cleaner, MX150QTD-6L, power 150 W), yielding a stock suspension. The stock suspension was washed with Milli-Q water three times to remove any Pt debris by repeated centrifugation (using Tarsons SPINWINTM MC 03 microcentrifuge at 5000 rpm for 5 minutes at room temperature), followed by re-dispersion. This washed suspension was once again centrifuged, the supernatant discarded, and the particles were redispersed in Milli-Q water to obtain a 1 wt% aqueous suspension of Janus particles [13,41]. To induce catalytic activity on the Pt side, appropriate quantities of H₂O₂ were added to the final Janus suspension, yielding overall H₂O₂ concentrations between 0.1 and 10 wt% in the suspension medium.

Substrate preparation: Clean silicon wafers were used as the hydrophilic substrate. For cleaning, the substrates were immersed in piranha solution (3:1 mixture of H_2SO_4 and H_2O_2), followed by thorough rinsing with Milli-Q water and drying with nitrogen gas before use. Hydrophobic substrates were fabricated using Sylgard 184 (a two-part cross-linkable polydimethylsiloxane (PDMS) elastomer; Dow Corning, USA) films. The oligomer (part A) to cross-linker (part B) ratio was maintained at 10:1 (wt/wt). The Sylgard mixture was poured into a clean glass petri dish and cured at 120 °C for 12 hours in a hot air oven for complete crosslinking, after which it was carefully peeled off [42] and cut into desired sizes.

Droplet drying: All drying experiments were conducted under controlled ambient conditions of 23 °C and 40 % relative humidity. We employed two distinct drying conditions for our experiments: open (where the substrate was kept open to the environment) and closed (where the substrate was placed in a closed Petri dish). 2 μL suspension droplets were carefully dispensed onto the substrates using a calibrated micropipette (Tarson). The drying dynamics were monitored in situ using a stereo zoom microscope (Olympus SZX16). Simultaneously, the evolution of the droplet contact angle was recorded using a contact angle goniometer (Attension Theta Flex- Biolin Scientific Optical Tensiometer) in sessile droplet mode, enabling quantitative analysis of wetting behaviour and evaporation kinetics. Droplet images were acquired at a frame rate of 2.3 frames per second, and were analysed using the OneAttension software. After complete evaporation, the final dried morphologies were imaged using scanning electron microscopy (SEM, Ultra Plus 4098 FESEM, Carl Zeiss) and atomic force microscopy (AFM, Oxford Instruments MFP-3D-bio-AFM in tapping mode, with resonant frequency of 157 kHz). All experiments were repeated a minimum of five times to ensure reproducibility of the results.

RESULTS AND DISCUSSION

Evaporation dynamics of passive Janus particle droplets on hydrophilic and hydrophobic flat substrates:

Figure 1 compares the evaporation dynamics and final deposit morphologies of droplets containing PS-Pt Janus particles in the absence of H_2O_2 fuel on hydrophilic and hydrophobic flat substrates. Under these conditions, particle motion arises solely from evaporation-driven capillary flows. As presented in Figures 1a1,a2,b1,b2, the entire drying regime can be divided into four zones: constant contact radius (CCR) mode (indicated in blue), constant contact angle

(CCA) mode (indicated in yellow), mixed mode (indicated in grey) and fast evaporation step (indicated in green) for both hydrophilic and hydrophobic flat substrates.

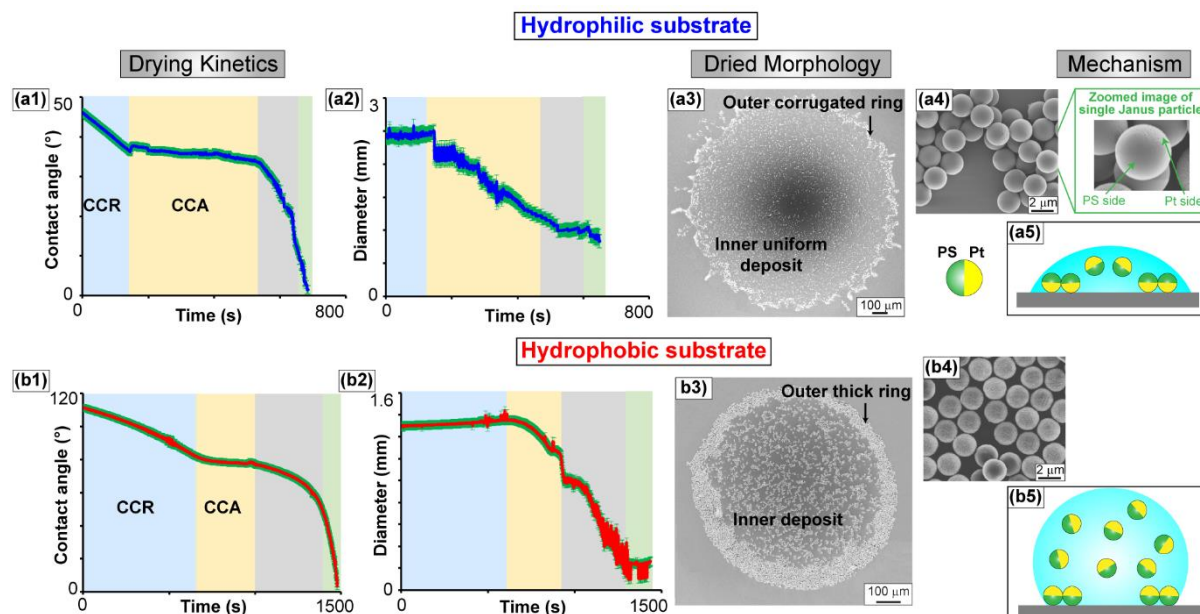


Figure 1 Evaporation dynamics and final dried morphologies of evaporating PS-Pt Janus particle droplets on (a) hydrophilic and (b) hydrophobic substrates in the absence of H_2O_2 fuel. (a1,b1) Evolution of droplet contact angle with time, highlighting pinned (CCR) and depinned (CCA) stages. The error bars are highlighted in green. (a2,b2) Corresponding changes in droplet diameter with time. (a3,b3) SEM images of the final dried deposits on hydrophilic and hydrophobic substrates. (a4,b4) Magnified SEM images showing orientations of the Janus particles, with zoomed in image of a single Janus particle highlighting the PS and Pt side, (a5,b5) schematic representation of particle orientation on hydrophilic vs hydrophobic substrates.

On hydrophilic substrates (Figures 1a1-a2), droplets initially evaporate in a pinned CCR mode, as indicated by a gradual decrease in contact angle accompanied by minimal variation in diameter of the droplet footprint (base diameter of the droplet on the surface immediately after dispensing). The strong solid-liquid affinity promotes rapid spreading and stabilises the three-phase contact line, producing a shallow droplet profile. As evaporation progresses, depinning occurs eventually and the droplet transitions to a constant contact angle (CCA) regime. Although the substrate is hydrophilic, depinning is facilitated by the progressive reorientation of the Janus particles near the contact line, as described in previous works [14,18]. Initially, particles anchor (pin) with their polymeric PS hemispheres on the substrate, stabilising the three-phase contact line. As the droplet thins, wettability contrast between PS and Pt generates asymmetric surface tension forces that drive reorientation, allowing the Pt caps to contact the substrate. Once sufficient particles reorient, contact-line depinning occurs despite the surface being hydrophilic. This evaporation dynamics is directly reflected in the final dried morphologies observed here (Figure 1a3-a4). Inspection of the acquired SEM image (Figure

1a4) after droplet drying reveals preferential exposure of the polymeric PS hemisphere, indicating that the Pt side contacts the substrate (the brighter and rough hemisphere is identified as the Pt side, and the darker smooth hemisphere as the PS side).

In contrast, droplets evaporating on hydrophobic substrates exhibit markedly different behaviour (Figures 1b1-b2). The initial contact angle is substantially larger, producing a taller and more curved droplet profile in which particles near the base are positioned closer to the triple phase contact line from the outset [16]. This enables rapid reorientation of the Janus particles such that the lower-energy polymeric PS hemispheres preferentially contact the substrate while the Pt caps remain exposed toward the air-liquid interface [43]. This early orientation allows the droplet to retain a pinned footprint for a significantly longer fraction of the drying process (blue region in Figures 1b1-b2). Depinning eventually occurs abruptly (yellow regions in the same figures). The prolonged pinned regime enhances the outward capillary flux, resulting in a thicker, more continuous outer ring in the final deposit (Figure 1b3). Corresponding SEM images reveal predominant exposure of the Pt hemispheres (Figure 1b4). The emergence of a mixed evaporation regime (grey region) in both cases arises from intermittent stick-slip motion driven by the orientation-dependent rearrangement of Janus particles at the contact line, causing both the contact angle and droplet footprint to decrease simultaneously before the final rapid evaporation stage. Notably, even in the absence of catalytic activity, the intrinsic anisotropy of Janus particles introduces an additional control pathway in droplet drying by enabling orientation-dependent adhesion and localised stress relaxation at the contact line.

Fuel-driven evaporation dynamics of catalytically active Janus particle droplets on hydrophilic substrates under open drying conditions:

Figure 2 displays modifications in the evaporation dynamics of active PS-Pt active Janus particle droplets on a hydrophilic flat substrate due to increase in H₂O₂ concentration (0.1-10 wt % in Milli-Q water) under open drying conditions. The drying kinetics evolve systematically with H₂O₂ concentration (Figures 2a1-f1). The entire drying regime has been divided into three zones: CCR mode (indicated in blue), mixed mode (indicated in grey) and fast evaporation (indicated in green). The magnified side-views of the evaporating droplets (insets), captured with a contact-angle goniometer, show the emergence of the O₂ bubbles (highlighted in the inset of Figure 2b1). Changes in the drying kinetics are mirrored in the intermediate top-view droplet images captured with an optical microscope (Figures 2a2-f2).

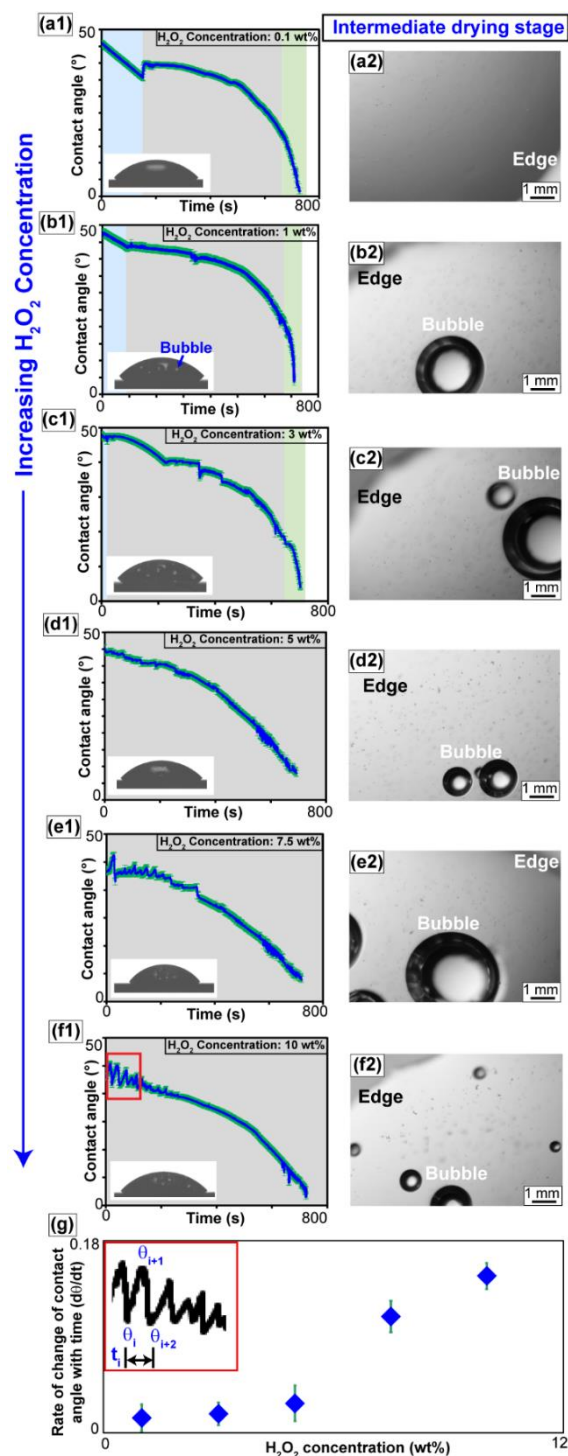


Figure 2 Drying kinetics of catalytically active Janus particle droplets on a flat hydrophilic substrate with increasing H_2O_2 concentrations: (a) 0.1 wt%, (b) 1 wt%, (c) 3 wt%, (d) 5 wt%, (e) 7.5 wt%, and (f) 10 wt%. (a1)-(f1): Evolution of the contact angle (θ) with time. The error bars calculated from five individual runs are highlighted in green. Insets show side views of the evaporating droplets. (a2)-(f2): Top-view optical microscope images captured at intermediate time, showing evolution of O_2 bubbles. (g) The rate of change of contact angle with time ($d\theta/dt$). Inset shows a schematic of the protocol followed to estimate $d\theta/dt$.

At low fuel concentrations (0.1-1 wt%, Figures 2a1-b1), the initial stage of evaporation is governed by capillary transport, during which the droplet remains pinned and follows a CCR

mode. This capillary flux sustains particle advection and produces an initially smooth decrease in contact angle. However, unlike the purely passive droplet in Figure 1a1, where the interface transitions from CCR to a CCA regime, the active system does not exhibit a clear CCA stage. Instead, the evaporation pathway enters a mixed mode following the initial pinned interval. This deviation arises because catalytic O_2 generation at the platinum caps begins to intermittently perturb the interface. Short-lived bubbles nucleate near the air-liquid interface (Figure 2b2). Their repeated formation disrupts the uniform stress distribution required to sustain a stable CCA regime. Each bubble locally modifies interfacial curvature and composition, generating transient surface-tension gradients. These gradients drive bubble-induced Marangoni flows, which momentarily disrupt the outward capillary flux [28]. Consequently, the contact-angle trajectory displays minor oscillations instead of a smooth trajectory. Capillarity still dominates the global drying dynamics in this low activity regime, but the interface is no longer purely passive. The combined action of outward evaporation-driven flow and intermittent bubble-mediated Marangoni recirculation produces a hybrid evaporation pathway. As the H_2O_2 concentration increases to intermediate levels (3-5 wt%, Figures 2c-d), measurable deviations from classical evaporation become apparent. The contact-angle curves develop fluctuations superimposed on the monotonic decay, indicating intermittent coupling between catalytic activity and interfacial curvature. Bubble nucleation becomes more frequent, and short-lived interfacial disturbances periodically modulate local stress distributions. This regime represents a transitional state in which catalytic O_2 generation begins to compete with evaporation-induced capillary stresses. The contact line still exhibits overall stability, but local pinning-depinning-repinning events become increasingly evident. At higher fuel concentrations (7.5-10 wt%, Figures 2e-f), the contact-angle evolution displays pronounced, high-frequency oscillations during both early and intermediate drying stages. These oscillations correspond to repeated cycles of bubble nucleation, growth, coalescence and bursts at or near the air-liquid interface. The magnitude of catalytic forces becomes sufficient to repeatedly disrupt the droplet surface, producing a highly irregular evaporation trajectory characterised by rapid curvature fluctuations and intermittent local depinning. In this regime, bubble-induced Marangoni stresses intermittently reverse or redistribute internal flow pathways, significantly reducing the effective pinning interval and accelerating the transition towards the terminal evaporation stage. Unlike the passive hydrophilic case where evaporation proceeds through well-defined CCR and CCA regimes governed solely by capillary and pinning forces, the active system exhibits activity-dependent deviations from classical behaviour. Even at low fuel concentrations, bubble-mediated interfacial perturbations suppress

the emergence of a stable CCA stage, while increasing catalytic activity progressively amplifies contact-angle fluctuations, enhances local depinning events, and shortens the effective pinned interval. Thus, catalytic O₂ generation introduces a dynamic, non-equilibrium control parameter that competes with evaporation-driven capillarity and fundamentally reshapes the drying pathway.

To quantify the degree of interfacial disturbance, the rate of change of contact angle with time ($d\theta/dt$) was extracted from the contact-angle trajectories and plotted as a function of H₂O₂ concentration (Figure 2g). As illustrated schematically in the inset of Figure 2g, each oscillatory rise and drop in the contact-angle (θ) was treated as an individual event. The magnitude of change between two successive extrema ($\theta_{i+1} - \theta_i$) was divided by the corresponding time interval (t_i), yielding a local $d\theta_i/dt_i$ for the i th segment. This procedure was repeated across multiple oscillation cycles, generating a set of discrete $d\theta_i/dt_i$ values. The final reported rate for a given H₂O₂ fuel concentration was obtained by averaging these segment-wise $d\theta_i/dt_i$ values: $\langle \frac{d\theta}{dt} \rangle = \frac{1}{N} \sum_{i=1}^N \frac{\theta_{i+1} - \theta_i}{t_i}$

The resulting trend obtained from our experiments reveals a systematic increase in the average $d\theta/dt$ with fuel concentration, indicating that interfacial curvature fluctuations become faster as catalytic O₂ generation intensifies. Overall, Figure 2 reveals a hierarchy of competing time scales. At low H₂O₂ concentrations, evaporation dominates and the droplet follows a primarily capillary-controlled pathway, whereas at intermediate concentrations, catalytic generation produces intermittent oscillations. At high concentrations, bubble generation overwhelms both processes, leading to sustained interfacial instabilities and a clear transition from capillary-dominated to catalytically-perturbed evaporation.

Fuel-dependent evaporation dynamics of catalytically active Janus droplets on hydrophobic substrates under open drying conditions:

Figure 3 quantifies how increasing H₂O₂ (fuel) concentration (0.1-10 wt% in Milli-Q water) progressively modifies the evaporation dynamics of PS-Pt active Janus particle droplets on a hydrophobic flat substrate, under open drying conditions. The drying kinetics evolve systematically with H₂O₂ concentration (Figures 3a1-f1). The entire drying regime has been divided into three zones: CCR mode (indicated in blue), mixed mode (indicated in grey) and fast evaporation (indicated in green). Insets show the magnified side-views of the evaporating droplets captured with a contact-angle goniometer. These changes are mirrored in the

intermediate top-view droplet images captured with an optical microscope (Figures 3a2-f2). To quantify activity induced perturbations of the droplet interface, the rate of change of contact angle with time ($d\theta/dt$) was determined (Figure 3g) using the protocol described earlier.

At low fuel concentrations (0.1-1 wt%, Figures 3a1-b1), the temporal decay of the contact angle follows a largely monotonic trend. The droplet maintains a higher initial and intermediate contact angle due to reduced substrate-liquid affinity and enhanced curvature imposed by hydrophobic wettability. Although the overall trajectory resembles passive hydrophobic evaporation, small fluctuations are already evident, indicating that weak catalytic O₂ generation perturbs the interface. Although no visually resolved O₂ bubbles appear during the drying process, we speculate that some O₂ bubbles are present which subtly reduces the pinning duration through localised bubble-induced Marangoni stresses. At intermediate fuel concentrations (3 wt%, Figure 3c1), evaporation departs markedly from smooth, monotonic behaviour. Following the initial pinned CCR stage, a distinct CCA regime is not established. Instead, the droplet transitions directly into a mixed mode. This behaviour is an indication of frequent bubble nucleation near the contact line. On the hydrophobic surface, particles and dissolved oxygen remain confined, promoting local supersaturation and delayed gas escape [44]. The resulting bubble growth induces localised interfacial deformation and spatially non-uniform surface tension gradients. These gradients generate bubble-induced Marangoni stresses that become comparable to the evaporation-driven capillary flux. Consequently, the contact line does not relax smoothly into a CCA regime but instead experiences repeated pinning-depinning-repinning events. The absence of a stable CCA phase therefore reflects the strong coupling between hydrophobic curvature, O₂ accumulation, and interfacial stress imbalance, which fragments the classical evaporation pathway into a dynamically mixed mode. At higher fuel concentrations (5-10 wt%, Figures 3d1-f1), evaporation becomes strongly oscillatory and temporally discontinuous. The contact-angle graph displays large-amplitude, abrupt drops, indicating repeated cycles of bubble nucleation, growth, coalescence, and detachment at or near the air-liquid interface. Unlike the hydrophilic case (Figures 2d1-f1), where oscillations are comparatively small, the hydrophobic geometry sustains these fluctuations over extended durations. Since hydrophobic substrates amplify local surface tension gradients and strengthen bubble-induced Marangoni stresses [31], the contact line does not recede smoothly but undergoes successive slip events, each associated with localised stress release following bubble detachment. The evaporation trajectory therefore consists of discrete relaxation episodes rather than a continuous decrease in curvature.

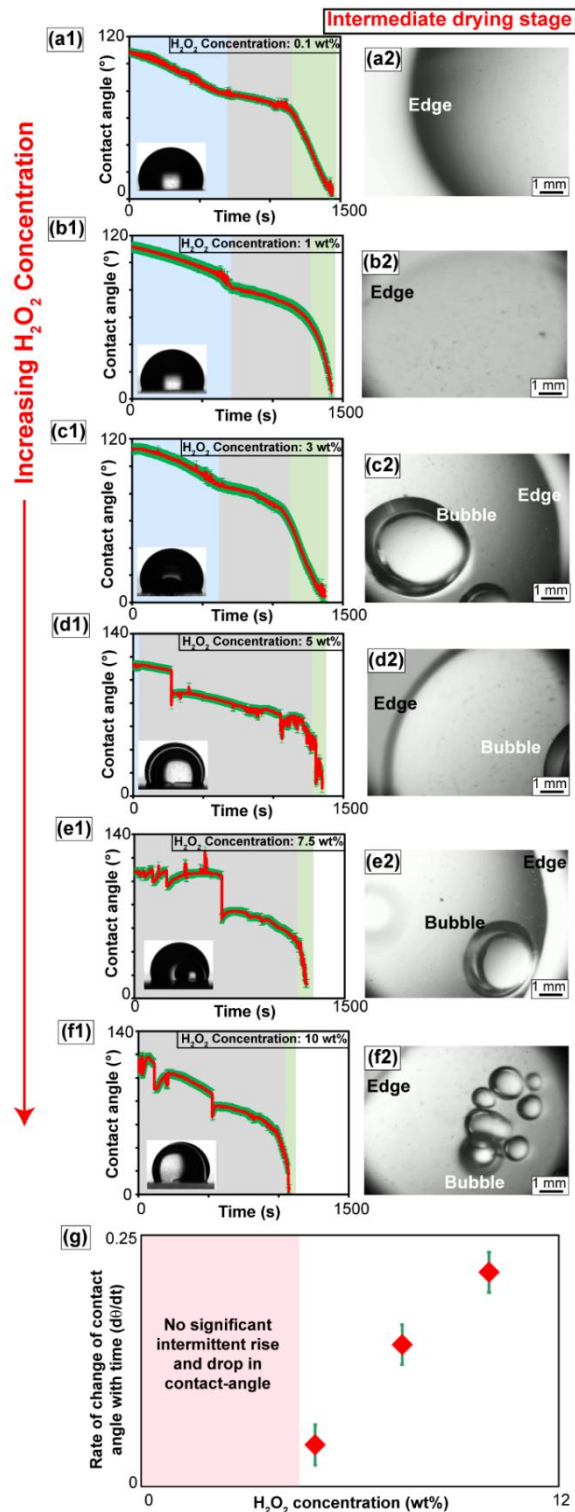


Figure 3 Drying kinetics of catalytically active Janus particle droplets on a hydrophobic substrate. with increasing H_2O_2 concentration: (a) 0.1 wt%, (b) 1 wt%, (c) 3 wt%, (d) 5 wt%, (e) 7.5 wt%, and (f) 10 wt%. (a1)-(f1): Evolution of contact angle with time. The error bars calculated from five individual runs are highlighted in green. (a2)-(f2): Top-view optical microscope images captured at intermediate time, showing evolution of O_2 bubbles. (g) The rate of change of contact angle with time ($d\theta/dt$).

$d\theta/dt$ plotted against H_2O_2 concentration (Figure 3g), shows a steeper increase compared to hydrophilic substrates. indicating larger fluctuations due to higher O_2 bubble activity on the

hydrophobic substrate. This provides a quantitative descriptor of the enhanced interfacial instability induced by the combined effects of catalytic O₂ generation and hydrophobicity.

Influence of bubble lifetime on deposition morphologies of catalytically active Janus droplets:

Figure 4 illustrates how the interplay between catalytic O₂ generation and vapour escape pathways governs particle organisation on both hydrophilic and hydrophobic substrates. Under open drying conditions on hydrophilic substrates (Figures 4a1-c1), low fuel concentrations (0-1 wt%) produce deposits with a relatively thin but well-defined peripheral ring, reflecting sustained outward capillary transport and weak Marangoni stresses. The annulus shows mild corrugation due to local particle interactions and discrete pinning sites [10], while the high-magnification insets reveal limited clustering, indicating that bubble-mediated perturbations remain transient and do not significantly disrupt radial flux. In contrast, under closed drying (Figures 4a2-c2), deposits become more spatially uniform at the same concentrations. The peripheral ring is less sharply defined and the interior particle density increases, consistent with restricted vapour diffusion, extended droplet lifetime, and reduced net outward capillary flow [28]. In contrast to the hydrophilic substrates discussed above, hydrophobic surfaces (Figures 4a3-c3) produce thicker, broader, and more sharply defined peripheral rings under open conditions, consistent with stronger and prolonged contact line pinning that sustains outward advection. Insets show dense particle packing along the boundary with some interior clustering, confirming dominant evaporation-driven transport. Under closed conditions, however, the annular band becomes less distinct even on the hydrophobic substrates, reflecting reduced radial flux and inward recirculation. Overall, the deposit morphology reflects the weak influence of catalytic bubbles, with substrate-dependent pinning governing peripheral accumulation even as limited bubble-mediated recirculation only modestly redistributes particles under prolonged (closed) drying conditions.

At intermediate fuel concentrations (3-5 wt%) under open drying (Figures 4d1-e1), hydrophilic substrates retain a discernible peripheral ring, but it develops corrugations and local discontinuities due to repeated bubble nucleation-burst cycles. Bubble-induced Marangoni stresses intermittently weaken the capillary-driven outward flux [28,31]. Under closed conditions (Figures 4d2-e2), restricted vapour diffusion and longer bubble lifetimes enhance interfacial deformation and recirculation, producing broader, more diffuse deposits with reduced annular sharpness and greater interior particle density. On hydrophobic substrates

(Figures 4d3-d4), the peripheral ring persists under open conditions but exhibits irregular thickening and corrugation from intermittent bubble-mediated pinning-depinning events. In closed systems, prolonged bubble residence further destabilises the annular boundary, yielding a non-uniform and partially redistributed deposit due to sustained Marangoni recirculation and delayed evaporation. Overall, at intermediate fuel concentrations, prolonged bubble lifetime and enhanced Marangoni stresses increasingly compete with capillary transport, progressively destabilising the peripheral ring, which is amplified under closed drying conditions and moderated by stronger contact-line pinning on hydrophobic substrates.

At high fuel concentrations (7.5-10 wt%), catalytic activity dominates the drying pathway and the contrast between open and closed environments becomes most pronounced. On hydrophilic substrates under open conditions (Figures 4f1-g1), rapid O₂ escape limits bubble residence time, suppressing sustained Marangoni recirculation and smoothing the deposit into a more spatially uniform morphology with a weakened or disappearing peripheral ring. In closed systems (Figures 4f2-g2), restricted gas escape prolongs bubble lifetime and promotes repeated growth-coalescence cycles, generating persistent surface tension gradients and cyclic pinning-depinning events that produce multiple concentric bands instead of a single annulus. On hydrophobic substrates under open drying (Figures 4e3-g3), the coherent ring destabilises into discrete, radially oriented protrusions, forming a star-like morphology driven by frequent, short-lived Marangoni bursts that redirect particle transport along radial pathways. Under closed conditions (Figures 4e4-g4), prolonged bubble residence enhances sustained interfacial deformation, leading to fragmented annular segments and increased inward redistribution rather than smooth concentric rings. Overall, at high fuel concentrations, bubble lifetime becomes the primary control parameter, with rapid gas escape in open systems favouring transient perturbations and uniform particle redistribution, while restricted escape in closed environments sustains interfacial deformation and drives complex, multi-banded or fragmented deposition patterns.

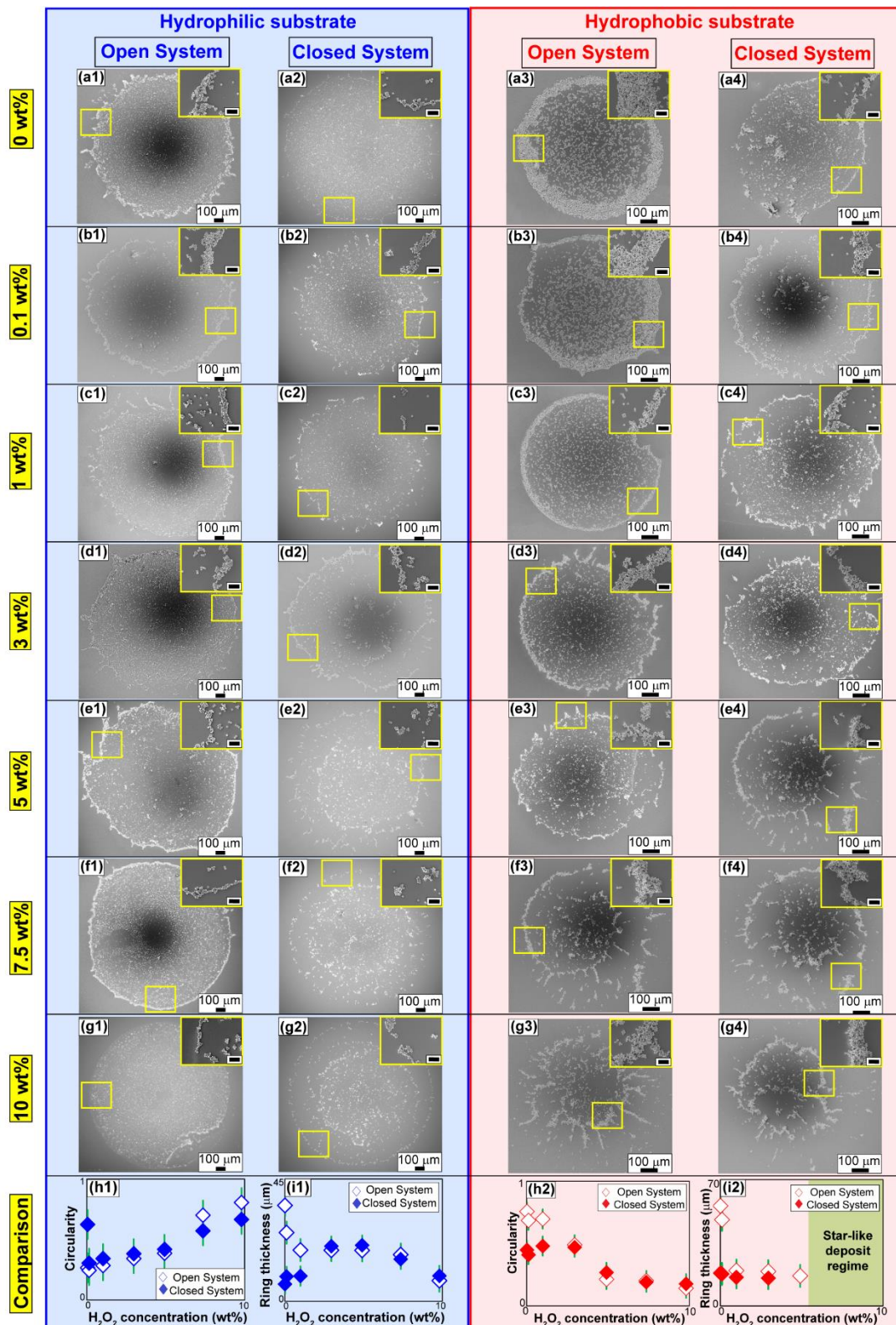


Figure 4 SEM images of final dried droplet deposits on hydrophilic and hydrophobic surface with increasing H_2O_2 concentrations: (a) 0 wt%, (b) 0.1 wt%, (c) 1 wt%, (d) 3 wt%, (e) 5 wt%, (f) 7.5 wt%, and (g) 10 wt%. (a1)-(g1), (a3)-(g3) respectively correspond to open drying conditions on hydrophilic and hydrophobic substrates. (a2)-(g2), (a4)-(g4) respectively correspond to closed drying conditions on hydrophilic and hydrophobic substrates. Insets show higher magnification views of selected regions to highlight microstructural details. The scale bar in the inset is 20 μm . Variation in (h) circularity and (i) ring thickness of the deposit morphologies with increasing H_2O_2 concentration.

The morphological trends are quantitatively reflected in the circularity and ring-thickness analysis (Figures 4h-i). Circularity was quantified in MATLAB by tracing the outer boundary of the dried deposit and computing the standard shape factor $C = 4\pi A/P^2$, (computed using the function `regionprops`) where A is the projected area and P is the perimeter (with $C=1$ corresponding to a perfect circle). Ring thickness was also determined using a MATLAB script by defining the outer and inner annular boundaries and calculating their radial separation, averaged over 20 measurements to account for local heterogeneity. On hydrophilic substrates, circularity increases with H_2O_2 concentration in both environments, particularly under open conditions at high fuel levels, consistent with the observed suppression of a sharply defined annulus and emergence of more spatially uniform deposits. In closed systems, elevated circularity reflects sustained bubble-driven recirculation that redistributes particles while maintaining overall footprint symmetry. In contrast, on hydrophobic substrates, circularity decreases progressively with increasing fuel concentration in both open and closed environments, consistent with the development of radial protrusions and fragmented boundaries. This loss of symmetry is amplified under closed conditions due to prolonged bubble residence and stronger interfacial disturbances. Ring-thickness data further distinguish deposit uniformity across the droplet footprint. On hydrophilic substrates under open drying, ring thickness decreases monotonically with increasing fuel concentration, reflecting progressive weakening of sustained capillary-driven edge accumulation. In closed systems, a non-monotonic trend emerges, with intermediate concentrations showing temporary thickening near the centre of the deposit. This is attributed to persistent recirculation and pinning-depinning events. Eventually, multi-ring structures dominate at high activity. On hydrophobic substrates, even minimal fuel addition sharply reduces thickness in both environments, indicating rapid disruption of edge-directed advection. At higher concentrations, thickness remains relatively similar as catalytic activity suppresses stable annular build-up. Overall, catalytic activity shifts the system from capillarity-dominated toward bubble lifetime-controlled redistribution, with substrate wettability and vapour confinement determining whether deposit uniformity is preserved or progressively destabilised.

Deposition heterogeneity revealed by AFM: role of wettability, activity, and evaporation environment

Figure 5 provides nanoscale topographical insight into the spatial heterogeneity of PS-Pt active Janus particle deposits by resolving local height distributions and clustering patterns using AFM. Measurements were performed at both the edge and centre of dried droplets on

hydrophilic and hydrophobic substrates, under open and closed evaporation environments, at representative low (1 wt%) and high (7.5 wt%) H_2O_2 concentrations. This mapping enables direct correlation between macroscopic deposit footprint morphology and particle-scale organisation.

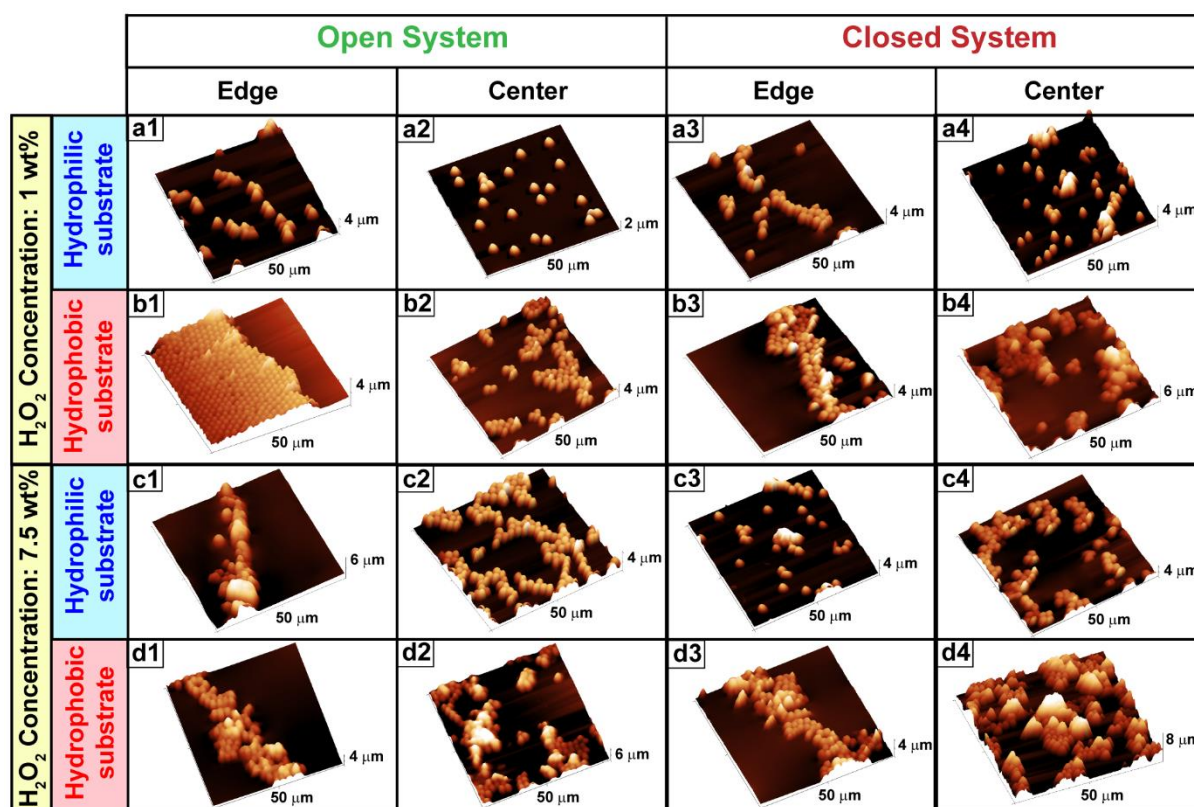


Figure 5 Representative AFM images of dried droplet deposits on hydrophilic and hydrophobic substrates at different H_2O_2 concentrations: (a1-a4) 1 wt% and (c1-d4) 7.5 wt%. Rows represent the substrate wettability: hydrophilic (a1-a4, c1-c4) and hydrophobic (b1-b4, d1-d4). Columns represent drying conditions: open (a1, a2, b1, b2, c1, c2, d1, d2) and closed (a3, a4, b3, b4, c3, c4, d3, d4). For each condition, AFM scans were taken at both the edge and centre of the droplet to capture spatial variations in deposition morphologies.

At low catalytic activity (1 wt% H_2O_2) on hydrophilic substrates, the AFM images under open conditions (Figures 5a1-a2) show relatively isolated particle islands at both the edge and centre, with limited lateral aggregation. The edge region displays slightly elongated clusters, whereas the centre retains sparse and evenly distributed particles. Under closed conditions (Figures 5a3-a4), both regions exhibit increased lateral clustering and broader height distributions, indicating that restricted vapour escape and prolonged droplet lifetime enhance particle-particle interactions. The difference between edge and centre becomes less pronounced in the latter case, reflecting partial redistribution driven by slower evaporation and mild Marangoni recirculation. On hydrophobic substrates at 1 wt% (Figures 5b1-b4), the heterogeneity is inherently stronger. Under open conditions, the edge region shows denser packing compared

to the centre, reflecting prolonged contact-line pinning and enhanced local accumulation. Under closed conditions, both edge and centre develop interconnected aggregates, with increased roughness contrast and reduced spatial separation between clusters. This indicates that unfavourable wetting amplifies boundary retention, while confinement promotes aggregation across the footprint rather than uniform spreading, because weaker solid-liquid affinity and higher interfacial curvature increase particle residence time near the interface and limit lateral stress relaxation.

At high catalytic activity (7.5 wt% H₂O₂), the AFM images reveal a marked transition from isolated deposits to continuous networked structures, indicating dominant bubble-mediated redistribution. On hydrophilic substrates under an open condition (Figures 5c1-c2), the edge region shows cluster coalescence, rather than isolated deposits as observed at low activity. The centre develops more interconnected cluster networks than observed at 1 wt% H₂O₂. The morphology on hydrophilic substrates under open condition reflects enhanced particle-particle interactions and intermittent redistribution driven by catalytic disturbances, but without clear directional alignment. Under closed conditions (Figures 5c3-c4), aggregation becomes more compact, particularly at the centre, where cluster coalescence reduces inter-cluster spacing. This arises from restricted vapour diffusion and prolonged bubble residence, which together extend the droplet lifetime and sustain bubble-induced Marangoni recirculation. The longer residence time increases the probability of particle-particle encounters and promotes repeated inward redistribution cycles, enabling neighbouring clusters to merge into larger aggregates rather than remain laterally dispersed [45,46]. In contrast, the edge region is characterised by discontinuous localised particle accumulation. On hydrophobic substrates at 7.5 wt%, heterogeneity reaches its maximum. Under open conditions (Figures 5d1-d2), the edge shows a uniform ring at some regions, while the centre exhibits clustered deposits reflecting rapid but spatially localised Marangoni bursts. Under closed conditions (Figures 5d3-d4), both edge and centre display densely packed, multi-level aggregates. The centre, in particular, develops structures indicative of repeated inward particle transport and coalescence. This morphology arises from the extended droplet lifetime and sustained internal flow loops in closed environments, which increase particle collision frequency and favour volumetric stacking rather than purely lateral spreading.

Overall, Figure 5 demonstrates that deposition heterogeneity is governed by the coupled action of wettability, catalytic activity and evaporation environment. Hydrophilic substrates at low activity favour isolated deposits, whereas hydrophobic substrates inherently amplify boundary

clustering. Increasing catalytic activity transforms discrete islands into networked structures through bubble-induced Marangoni flows, while confinement further enhances vertical aggregation by extending bubble residence time. The AFM analysis thus reveals that the transition from capillary-dominated to catalytically perturbed drying is manifested not only in global footprint morphology but also in cluster connectivity and edge-centre roughness contrast at the nanoscale.

Conclusions

This study identifies bubble residence time as a control parameter governing evaporation dynamics, interfacial stability, and final deposition morphology of catalytically active Janus particle droplets on flat surfaces. Through systematic variation of hydrogen peroxide concentration, evaporation environment and surface wettability, we show that active droplet drying is regulated by a set of coupled mechanisms. These mechanisms are evaporation-driven capillary transport, Marangoni stress relaxation, and catalytic O₂ generation.

At low activity, evaporation-controlled capillary flows dominate on both hydrophilic and hydrophobic substrates, yielding smooth contact-angle decay and relatively ordered peripheral deposits. With increasing activity, catalytic forces progressively perturb the interfacial stress balance, introducing intermittent oscillations and mixed transport regimes characterised by competing inward and outward flows. Beyond a critical activity threshold, bubble-mediated disturbances become the primary driver of interfacial dynamics, producing rapid curvature fluctuations, shortened pinning intervals, and increasingly heterogeneous deposition patterns. Hydrophilic substrates mitigate these effects through enhanced wetting and faster stress relaxation, whereas hydrophobic substrates prolong interfacial residence time and O₂ retention, thereby lowering the instability threshold and amplifying particle disorder.

Time-resolved contact-angle analysis with structural characterisation also establishes the key role of bubble growth and burst cycles as the decisive parameter that governs the transition from capillary-dominated to catalytically perturbed drying in active Janus droplets. The rate of contact-angle change and deposit circularity emerge as robust quantitative descriptors of interfacial destabilisation, linking dynamic evaporation pathways to final deposition outcomes. In summary, our results recast evaporating colloidal Janus droplets as chemically responsive interfaces rather than passive transport systems. The design framework developed here provides practical guidelines for tuning pattern formation in reactive coatings, printing, and

microreactor platforms, while contributing to a deeper understanding of nonequilibrium interfacial phenomena in active colloidal matter.

Acknowledgements: We would like to thank Mr. Yatheendran K. M. for assistance with SEM and AFM imaging.

Research ethics: Not applicable.

Informed consent: Not applicable.

Author contributions: Meneka Banik: Conceptualisation, Data curation, Methodology, Validation, Formal analysis, Investigation, Writing - Original Draft, Visualisation.

Ranjini Bandyopadhyay: Methodology, Validation, Resources, Data curation, Writing - Review & Editing, Supervision, Project administration, Funding acquisition.

Use of Large Language Models, AI and Machine Learning Tools: None declared.

Conflict of interest: The authors state no conflict of interest.

Research funding: We would like to thank Raman Research Institute, Bangalore for funding the research.

Data availability: The data that support the findings of this study are available on request.

References

1. R. D. Deegan, O. Bakajin, T. F. Dupont, G. Huber, S. R. Nagel, and T. A. Witten, "Capillary flow as the cause of ring stains from dried liquid drops," *Nature*, vol. 389, no. 6653, pp. 827–829, 1997.
2. R. D. Deegan, "Pattern formation in drying drops," *Phys. Rev. E*, vol. 61, no. 1, pp. 475–485, 2000.
3. H. Hu and R. G. Larson, "Evaporation of a sessile droplet on a substrate," *J. Phys. Chem. B*, vol. 106, no. 6, pp. 1334–1344, 2002.
4. R. G. Larson, "Transport and deposition patterns in drying sessile droplets," *AIChE J.*, vol. 60, no. 5, pp. 1538–1571, 2014.
5. H. Hu and R. G. Larson, "Marangoni effect reverses coffee-ring depositions," *J. Phys. Chem. B*, vol. 110, no. 14, pp. 7090–7097, 2006.

6. W. D. Ristenpart, P. G. Kim, C. Domingues, J. Wan, and H. A. Stone, "Influence of substrate conductivity on circulation reversal in evaporating drops," *Phys. Rev. Lett.*, vol. 99, pp. 234502, 2007.
7. K. Sefiane, "Patterns from drying drops," *Adv. Colloid Interface Sci.*, vol. 206, pp. 372–381, 2014.
8. B. Derby, "Inkjet printing of functional and structural materials: Fluid property requirements, feature stability, and resolution," *Annu. Rev. Mater. Res.*, vol. 40, pp. 395–414, 2010.
9. J. Park and J. Moon, "Control of colloidal particle deposit patterns within picoliter droplets ejected by ink-jet printing," *Langmuir*, vol. 22, no. 8, pp. 3506–3513, 2006.
10. P. J. Yunker, T. Still, M. A. Lohr, and A. G. Yodh, "Suppression of the coffee-ring effect by shape-dependent capillary interactions," *Nature*, vol. 476, no. 7360, pp. 308–311, 2011.
11. S. Michelin and E. Lauga, "Phoretic self-propulsion at finite Péclet numbers," *J. Fluid Mech.*, vol. 747, pp. 572–604, 2014.
12. J. L. Moran and J. D. Posner, "Phoretic self-propulsion," *Annu. Rev. Fluid Mech.*, vol. 49, pp. 511–540, 2017.
13. A. Walther and A. H. E. Müller, "Janus particles: Synthesis, self-assembly, physical properties, and applications," *Chem. Rev.*, vol. 113, no. 7, pp. 5194–5261, 2013.
14. B. P. Binks and P. D. I. Fletcher, "Particles adsorbed at the oil–water interface: A theoretical comparison between spheres of uniform wettability and Janus particles," *Langmuir*, vol. 17, no. 16, pp. 4708–4710, 2001.
15. J. Zhang, B. A. Grzybowski, and S. Granick, "Janus particle synthesis, assembly, and application," *Langmuir*, vol. 33, no. 28, pp. 6964–6977, 2017.
16. M. Banik, S. Sett, C. Bakli, A. K. Raychaudhuri, S. Chakraborty, and R. Mukherjee, "Substrate wettability guided oriented self-assembly of Janus particles," *Sci. Rep.*, vol. 11, pp. 1182, 2021.
17. Q. Xie, G. B. Davies, and J. Harting, "Direct assembly of magnetic Janus particles at a droplet interface," *ACS Nano*, vol. 11, no. 11, pp. 11232–11239, 2017.
18. S. Jiang and S. Granick, "Janus balance of amphiphilic colloidal particles," *J. Chem. Phys.*, vol. 127, pp. 161102, 2007.
19. S. J. Ebbens and J. R. Howse, "In pursuit of propulsion at the nanoscale," *Soft Matter*, vol. 6, no. 4, pp. 726–738, 2010.

20. S. Das, A. Garg, A. I. Campbell, J. Howse, A. Sen, D. Velegol, R. Golestanian, and S. J. Ebbens, "Boundaries can steer active Janus spheres," *Nat. Commun.*, vol. 6, pp. 8999, 2015.
21. H. Hu and R. G. Larson, "Analysis of the microfluid flow in an evaporating sessile droplet," *Langmuir*, vol. 21, no. 9, pp. 3963–3971, 2005.
22. D. Mampallil and H. B. Eral, "A review on suppression and utilization of the coffee-ring effect," *Adv. Colloid Interface Sci.*, vol. 252, pp. 38–54, 2018.
23. H. Y. Erbil, "Evaporation of pure liquid sessile and spherical suspended drops: A review," *Adv. Colloid Interface Sci.*, vol. 170, pp. 67–86, 2012.
24. D. Bonn, J. Eggers, J. Indekeu, J. Meunier, and E. Rolley, "Wetting and spreading," *Rev. Mod. Phys.*, vol. 81, pp. 739–805, 2009.
25. P. G. de Gennes, "Wetting: statics and dynamics," *Rev. Mod. Phys.*, vol. 57, pp. 827–863, 1985.
26. R. G. Picknett and R. Bexon, "The evaporation of sessile or pendant drops in still air," *J. Colloid Interface Sci.*, vol. 61, pp. 336–350, 1977.
27. K. S. Birdi, D. T. Vu, and A. Winter, "The evaporation of a liquid drop on a solid surface," *J. Phys. Chem.*, vol. 93, pp. 3702–3703, 1989.
28. K. Singh, P. Kumar, H. Raman, H. Sharma, and R. Mangal, "Tailoring the coffee ring effect by chemically active Janus colloids," *ACS Appl. Eng. Mater.*, vol. 3, pp. 275–285, 2025.
29. W. E. Uspal, M. N. Popescu, S. Dietrich, and M. Tasinkevych, "Self-propulsion of a catalytically active particle near a planar wall," *Soft Matter*, vol. 11, pp. 434–438, 2015.
30. S. Thutupalli, R. Seemann, and S. Herminghaus, "Swarming behavior of simple model squirmers," *New J. Phys.*, vol. 13, pp. 073021, 2011.
31. M. Banik and R. Bandyopadhyay, "Bubble-driven flow transitions in evaporating active droplets on structured surfaces," *arXiv* 2511.22423, 2025.
32. R. Malinowski, G. Volpe, I. P. Parkin, and G. Volpe, "Dynamic control of particle deposition in evaporating droplets," *J. Phys. Chem. Lett.*, vol. 9, no. 3, pp. 659–664, 2018.
33. I. Buttinoni, J. Bialké, F. Kümmel, H. Löwen, C. Bechinger, and T. Speck, "Dynamical clustering and phase separation in suspensions of self-propelled colloidal particles," *Phys. Rev. Lett.*, vol. 110, pp. 238301, 2013.

34. J. R. Howse, R. A. L. Jones, A. J. Ryan, T. Gough, R. Vafabakhsh, and R. Golestanian, "Self-motile colloidal particles: From directed propulsion to random walk," *Phys. Rev. Lett.*, vol. 99, pp. 048102, 2007.
35. J. G. Gibbs and Y.-P. Zhao, "Autonomously motile catalytic nanomotors by bubble propulsion," *Appl. Phys. Lett.*, vol. 94, pp. 163104, 2009.
36. H.-J. Butt, J. Liu, K. Koynov, B. Straub, C. Hinduja, I. Roismann, R. Berger, X. Li, D. Vollmer, W. Steffen, and M. Kappl, "Contact angle hysteresis," *Curr. Opin. Colloid Interface Sci.*, vol. 59, pp. 101574, 2022.
37. R. Adkins, I. Kolvin, Z. You, S. Witthaus, M. C. Marchetti, and Z. Dogic, "Dynamics of active liquid interfaces," *Science*, vol. 377, no. 6606, pp. 768–772, 2022.
38. E. B. Dussan, "On the spreading of liquids on solid surfaces: Static and dynamic contact lines," *Annu. Rev. Fluid Mech.*, vol. 11, pp. 371–400, 1979.
39. A. Mozaffari, N. Sharifi-Mood, J. Koplik, and C. Maldarelli, "Self-diffusiophoretic colloidal propulsion near a solid boundary," *Phys. Fluids*, vol. 28, pp. 053107, 2016.
40. N. D. Denkov, O. D. Velev, P. A. Kralchevsky, I. B. Ivanov, H. Yoshimura, and K. Nagayama, "Mechanism of formation of two-dimensional crystals from latex particles on substrates," *Langmuir*, vol. 8, no. 12, pp. 3183–3190, 1992.
41. A. Perro, S. Reculosa, S. Ravaine, E. Bourgeat-Lami, and E. Duguet, "Design and synthesis of Janus micro- and nanoparticles," *J. Mater. Chem.*, vol. 15, pp. 3745–3760, 2005.
42. M. Banik and R. Shenhar, "Nanoparticle assembly by transient topography induced by applying soft lithography to block copolymer films," *Soft Matter*, vol. 20, pp. 4035–4042, 2024.
43. B. M. Weon and J. H. Je, "Self-pinning by colloids confined at a contact line," *Phys. Rev. Lett.*, vol. 110, pp. 028303, 2013.
44. A. Al-Sharafí, B. S. Yilbas, A. Z. Sahin, H. Ali, and H. Al-Qahtani, "Heat transfer characteristics and internal fluidity of a sessile droplet on hydrophilic and hydrophobic surfaces," *Appl. Therm. Eng.*, vol. 108, pp. 628–640, 2016.
45. I. Theurkauff, C. Cottin-Bizonne, J. Palacci, C. Ybert, and L. Bocquet, "Dynamic clustering in active colloidal suspensions with chemical signaling," *Phys. Rev. Lett.*, vol. 108, pp. 268303, 2012.
46. M. Jalaal, B. ten Hagen, H. Le The, C. Diddens, D. Lohse, and Á. Marin, "Interfacial aggregation of self-propelled Janus colloids in sessile droplets," *Phys. Rev. Fluids*, vol. 7, pp. 110514, 2022.

Graphical Abstract:

